energies

MDPI

Article

Feasibility Investigation of Attitude Control with Shape Memory Alloy Actuator on a Tethered Wing

Yufei Zhu [1,*], Ryohei Tsuruta [2], Rikin Gupta [1] and Taewoo Nam [1]

[1] Future Mobility Research Department, Toyota Research Institute North America, Ann Arbor, MI 48105, USA
[2] Frontier Research Center, Toyota Motor Corporation, Toyota 471-8571, Aichi, Japan
* Correspondence: yufei.zhu@toyota.com

Abstract: This study is aimed at assessing the feasibility of employing an innovative, smart-material-based control effector for an inflatable wing. A shape memory alloy (SMA) actuator is primarily investigated as a control effector in this work for its advantages of a simple actuation mechanism and a high force-to-weight ratio. This paper presents the design, control strategy and simulation results of the SMA actuator used as a stability augmentation system for a small-scale prototype kite. Stable flight of the kite is achieved during open wind tunnel tests using the SMA actuator. Based on experimental and simulation analyses, it is evident that the current SMA actuator is better for low-frequency actuations rather than stability augmentation purposes, as its performance is sensitive to practical conditions. The study also discusses potential improvements and applications of the SMA actuator.

Keywords: shape memory alloy; flight control; airborne wind energy harvesting

Citation: Zhu, Y.; Tsuruta, R.; Gupta, R.; Nam, T. Feasibility Investigation of Attitude Control with Shape Memory Alloy Actuator on a Tethered Wing. *Energies* **2023**, *16*, 5691. https://doi.org/10.3390/en16155691

Academic Editor: Chunhua Liu

Received: 15 June 2023
Revised: 25 July 2023
Accepted: 27 July 2023
Published: 29 July 2023

1. Introduction

A research team at the Toyota Research Institute of North America (TRINA) is investigating the feasibility of a high altitude aerial platform called "Mothership" [1]. This visionary air vehicle, essentially a large-scale kite made of an advanced inflatable structure, can offer unparalleled endurance and station keeping capabilities [2–5] that will make it suitable for missions such as large-scale airborne wind energy (AWE) harvesting [2], real-time atmospheric data acquisition and broadcasting, high-speed communication relays and disaster relief (Figure 1). The platform may serve as an incubator of various new technologies, encompassing novel actuators, sensors and lightweight structures. The wing design with a high aspect ratio and the absence of a vertical tail minimizes the aerodynamic drag at the cost of a low lateral directional stability, requiring a stability augmentation system. Furthermore, the kite must be capable of a certain degree of controlled maneuvering to ensure mission effectiveness and operation safety. Therefore, an active flight control system must be investigated. Installation of conventional flight control actuators generally requires rigid mounting structures and a firm hinge line to ensure control precision and to avoid control binding. It is a challenge to meet such design requirements when applying a conventional control mechanism to an inflatable structure. Hence, camber morphing techniques such as fishbone [6,7] and flexible rib [8] have been investigated as substitutions for their intact wing profile. Though they minimize drag by eliminating sudden flow separation along the airfoil camber, these hinge-line-free configurations require additional airfoil structures embedded in the wing section, which is difficult to achieve in an inflatable structure. Instead, we successfully installed servo motors onto the fabric envelope of a small-scale inflatable kite and demonstrated fly-by-wire control for stability augmentation and cross wind flight [3,4], utilizing concepts inspired by bird feathers [9]. However, mounting a rigid actuator becomes increasingly challenging as the kite size and required control power grow. This warrants investigations into innovative flight control actuators that can be more easily distributed and integrated into fabric-based structures.

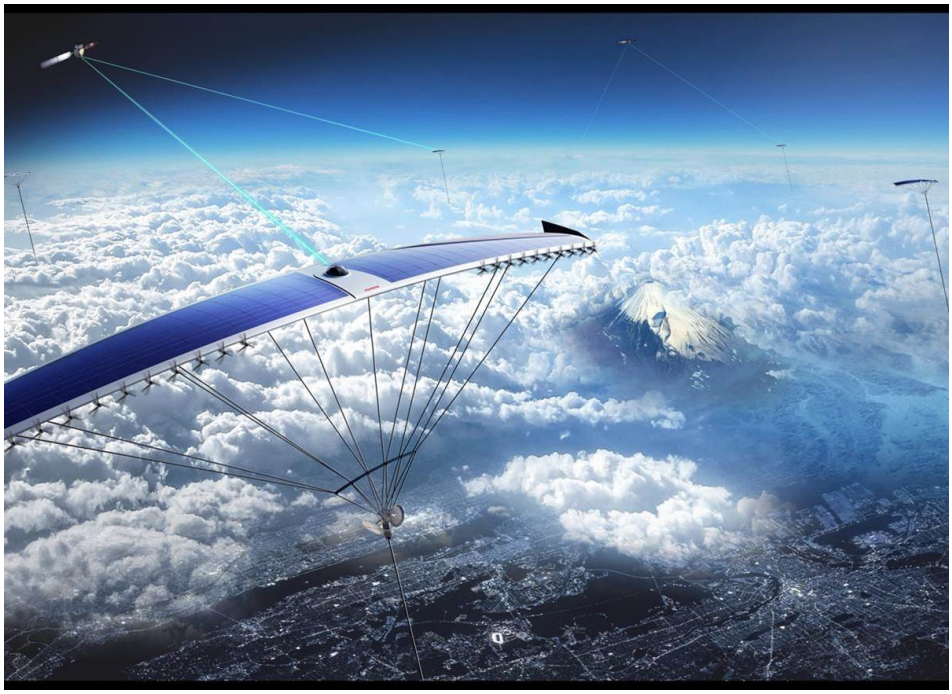

Figure 1. Artistic impression of the Mothership kite [1].

In robotics, assorted programmable materials have been studied for decades to develop soft actuators of high compliance and flexibility that may overcome the shortcomings of conventional actuators. Ample research [10–12] has been performed to investigate the applicability of soft actuators in diverse engineering areas. As soft actuators have vastly different characteristics, it is not always easy to find one that best fits a specific application area. The selection process can be facilitated by comparing candidate soft actuators in terms of the key attributes that determine soft actuators' performances and physical characteristics [13–16]. Such attributes are often computed in normalized metrics as shown in Figure 2, which allows a fair comparison independent of the application scale.

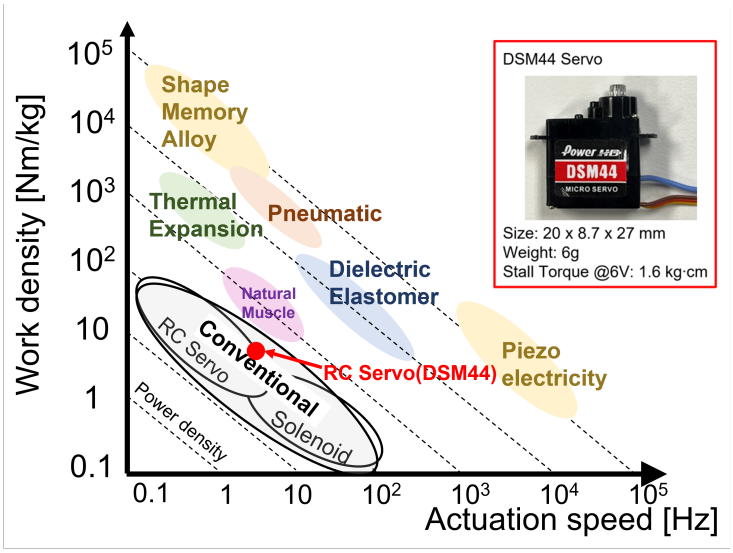

Figure 2. Work density versus actuation speed of smart material actuators. The performance of the RC servos utilized in [3,4] is compared with other actuators. The servo specs are from Pololu Robotics and Electronics [17].

Figure 2 compares many soft actuators in terms of actuation speed and work density, using data from previous research by Rich et al. [16] as well as in-house experimental results

from our group. The work density in the figure is defined as the ratio of the work done by the actuator and the actuator mass. Figure 2 also includes a high-frequency RC servo that we utilized to deflect control surfaces for a kite in previous research [3,4]. According to Figure 2, the piezoelectric actuator, dielectric elastomer actuator (DEA) and shape memory alloy (SMA) actuator appear to be good candidates to replace the RC servo.

Out of the three soft actuator candidates, the piezoelectric actuator has the highest actuation frequency. Fichera et al. [18] achieved high-bandwidth airfoil camber morphing by actuating the piezoelectric patch on the trailing edge. The 300 mm chord length wing section reached a tip deflection of 15 mm, resulting in an equivalent torque of 0.1 Nm that effectively controlled the wing's aeroelastic behavior and flight mechanics. The relatively moderate displacement of the presented piezoelectric actuators necessitates the arrangement of multiple rows of these actuators to achieve the concept proposed in [18] on a large-scale wing. As a matter of fact, the displacements of piezoelectric actuators are typically not significant since strains from piezoelectric materials are often too small to be directly useful. Furthermore, certain mechanisms have to be created to amplify these strains [19]. For example, FlexSys [20] demonstrates an alternative morphing scheme realized by a combination of a piezoelectric actuator and the compliant mechanism. Compared with piezoelectric actuators, DEAs have a lower but still acceptable actuation speed and a higher work density, making them a better candidate to replace the RC servo. Shintake et al. [21] applied an artificial muscle actuator to control the aerodynamic surface deflection of a UAV. Capitalizing on the large deformation and high response speed of DEAs, the artificial muscle actuator produced a control power sufficient for open field flights. Despite all the advantages, the stability and reliability of DEAs has not matured enough. The rates of structural failure are prohibitively high for a practical application on a large-scale inflatable wing [22,23].

Attending to the shortcomings of piezoelectric actuators and DEAs, this work focuses on actuators made of the third candidate: SMA wires. All three candidate actuators can achieve the embodiment concept that increases aerodynamic efficiency by eliminating the flow-disturbing hinge lines between the trailing edge and control surfaces. Compared to the other two actuator options, SMA wires offer several advantages such as a light weight, a high force-to-weight ratio and high durability [24]. Although SMA actuators are much slower than piezoelectric actuators, certain SMA actuators can achieve an actuation bandwidth of up several hertz, which is close to the operating frequency of RC servos. In addition, the high-voltage operation of piezoelectric actuators and DEAs may require additional voltage converters, which can significantly offset the lightweight benefits of these actuators. On the contrary, SMA actuators' operation voltages are noticeably lower than the ones required by piezoelectric actuators and DEAs. The typical supply voltages required for a SMA range between 12 V and 48 V in the automotive sector and between 110 V and 125 V in the aerospace industry [25]. Furthermore, SMA wires can be easily controlled with electrical signals, which significantly reduces the actuator's complexity and size [14]. Due to these benefits, SMA actuators have been extensively studied for aerospace applications, particularly in the field of aerostructure morphing [26–28]. Besides the rigid wing structure, two morphing approaches were proposed by Simpson et al. [29] to warp the inflatable wing section using SMA wires. A considerable effective flap deflection angle was achieved by SMA actuation in bench tests.

Despite SMA's widespread use in adaptive structures, there has been little development of SMA-wire-based flight control systems. Using its advantages of a light weight and a high force output, conventional servo motors may be replaced by SMA wires. Brennison et al. [30] introduced a flight control system that uses a potentiometer-based feedback control SMA actuator to deflect the rudder. Their work utilized a 0.003 inch (76.2 μm) diameter SMA that produced 7.5 oz in (0.54 kg·cm) of torque, which was sufficient for high-bandwidth actuation of a rudder in a conventional wing–tail arrangement with a relatively low hinge moment requirement. Considering the Toyota Mothership test kite's extended application size and flight envelope, a more powerful and sophisticated SMA

actuator is necessary to fulfil its large hinge moment requirement. This paper presents a unique control scheme to address the cooling issue associated with the use of thicker SMA wires for high-bandwidth actuation. In addition, a low-profile magnet-based feedback solution is presented as a replacement for the demodulator/potentiometer circuit used in [30], which is difficult to mount on an inflatable wing.

2. Stability Augmentation System of the Proof of Concept Kite

The goal of this work is to design, build and test an SMA actuator for use in the stability augmentation system (SAS) of a tethered kite. The design and integration of the SMA actuator is explained in the present section. To evaluate the performance of the SAS, the kite was flown in a custom-built open wind tunnel, while flight data were collected. An actuation mechanism was introduced to convert translational motions of SMA wire into rotational motions of the control surface. The displacement of the SMA wire was controlled by an onboard flight computer to ensure the accuracy of the control surface deflection. The flight computer is also responsible for kite stabilization during flight.

2.1. Test Platform and Prior Tests

A laser-cut foam kite was used as the test platform to investigate the SMA actuator, with an NACA 2414 airfoil shape selected. Table 1 displays the geometric properties of the test kite. As shown in Figure 3, the test kite is outfitted with two ailerons as control surfaces.

Table 1. Test kite geometric parameters.

Test Kite Geometric Parameters	
Wing Area (m^2)	1.6
Span (m)	3.4
MAC (m)	0.5
Dihedral (deg)	5.0
Leading Edge Sweep (Deg)	24.0
Test Kite Control Surface Geometric Parameters	
Span (m)	0.43
Root Chord (m)	0.11
Tip Chord (m)	0.09
Area (m^2)	0.04

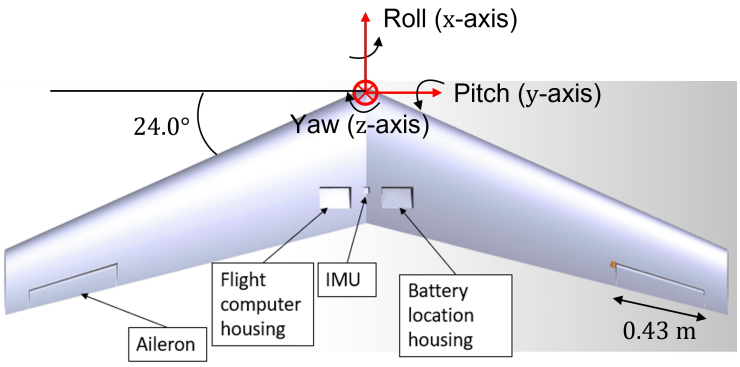

Figure 3. Test kite geometry and body frame definition.

The flight tests were conducted in a custom-built open wind tunnel, which was composed of a 3-by-9 matrix of fans, as shown in Figure 4a. The wind tunnel generated a quasi-steady flow field at 7 m/s within a range of a few meters. As am in-house wind tunnel customized by off-the-shelf duct fans, incidental flow disturbances were inevitably

generated by many sources, such as the installation gap between each fan. However, applying flow perturbation to the kite also helped to evaluate the flight controller's robustness. Figure 5a displays the flight-ready kite in the wind tunnel.

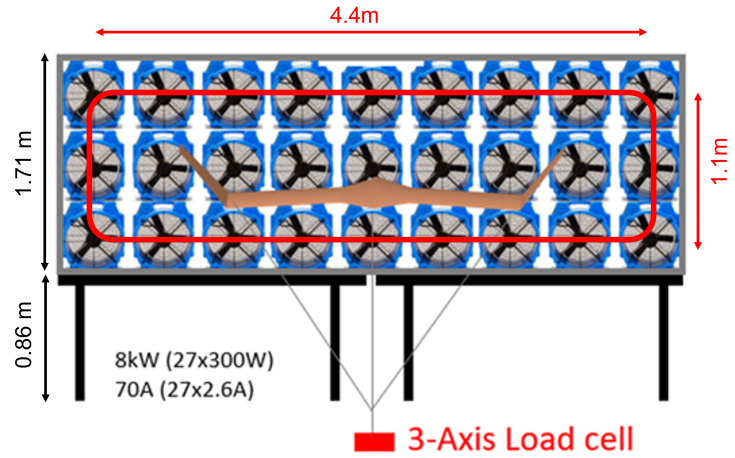

(**a**) Artistic impression of the custom−built wind tunnel test.

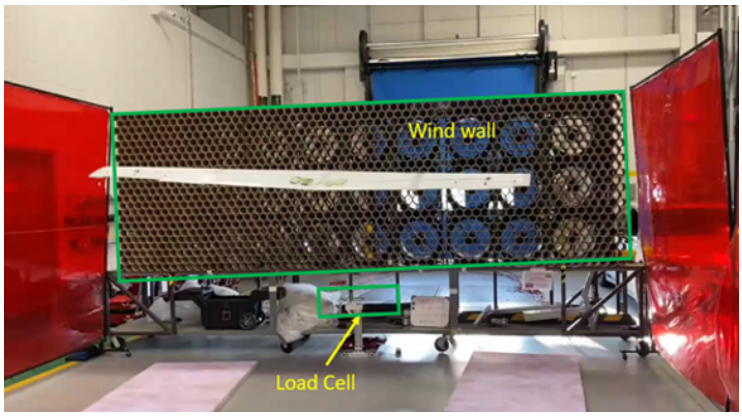

(**b**) Actual flight test conducted in the custom-built wind tunnel.

Figure 4. The custom−built wind tunnel for flight control system verification.

Initially, conventional servos were installed as the aileron deflection actuators to verify the effectiveness of the in-house developed attitude controller. The details of the control algorithm executed are discussed in the authors' previous work [3]. The kite was successfully stabilized during flight tests using a Linear-Quadratic Regulator (LQR) and Single-Input Single-Output (SISO) controllers with the ailerons actuated between −25 and +25 °. With equilibrium flight achieved by the attitude controller, the aileron output was limited to positive angles, emulating the SMA's contraction motion that can only deflect control surfaces upward. To simplify the naming convention, the mode in which the aileron deflects only upwards is referred to as the "spoiler mode". With controller gains tuned accordingly, the test kite accomplished trim flight in spoiler mode, with control surface deflections between 0° and 25° (Figure 5b). In terms of control authority, it appears feasible to replace servo motors with SMA actuators that can generate restoring moments from spoiler deflections.

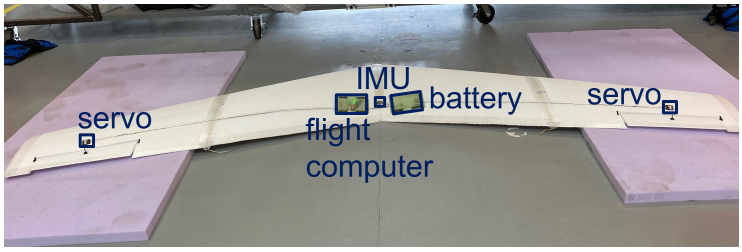

(**a**) Test kite undertaking a wind tunnel test in servo configuration.

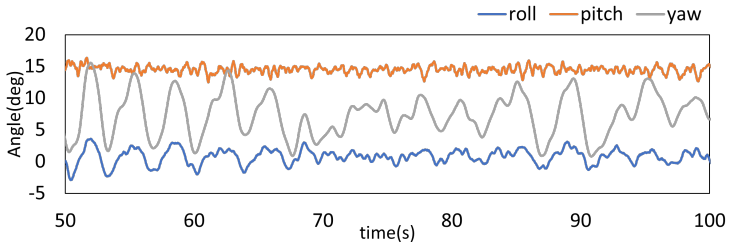

(**b**) Test kite (aileron mode) attitude in the wind tunnel test.

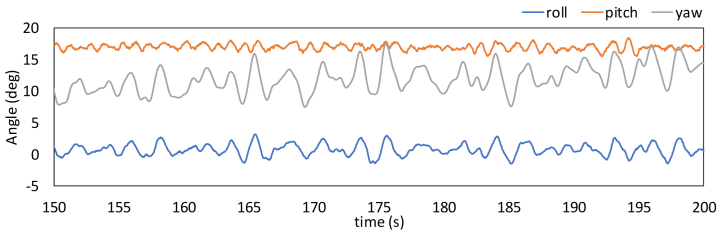

(**c**) Test kite (spoiler mode) attitude in wind tunnel test.

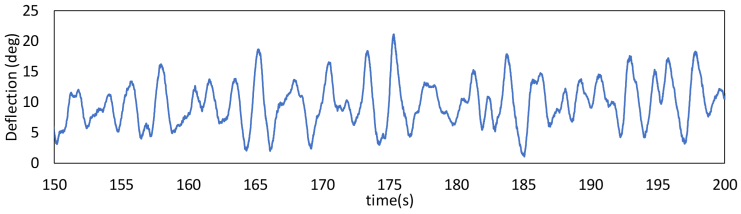

(**d**) Test kite control surface deflection in spoiler mode.

Figure 5. The setup and results of the attitude controller verification test in the wind tunnel.

2.2. SMA Actuation Configuration

An SMA wire contracts to a pre-defined, stress-dependent length when the wire is heated due to the shape memory effect (SME). Specifically, applying a voltage across the wire generates Joule heat that induces a crystalline phase transformation from martensite to austenite. When the voltage is removed, the wire gradually expands to its original length during heat dissipation. An SMA wire typically exhibits a 4–8% strain decrease in the high temperature (austenite) phase [31,32]. As such, SMA wires are well suited for use as linear actuators. However, the involvement of nonlinearity, hysteresis and time-varying parameters in SMA phase transformation dynamics makes it difficult to achieve high-performance actuation [33]. Several methods have been proposed to model the SMA dynamics in order to reflect its actuation with minimum errors [34–36]. In addition, control schemes such as self-tuning fuzzy PID [37], Sliding Mode Control (SMC) [38] and neural network model predictive control [39] have also been studied to improve SMA actuator performance. According to Zhang et al. [33], governed by proper models and control algorithms, more than 89% of SMA tracking errors can be eliminated in a well-controlled environment.

Although accurate SMA position tracking has been achieved in a lab environment (constant load, room temperature, adequate DAQ system, low actuation frequency, etc.),

it is still an open problem to effectively reject the SMA modeling errors under practical conditions [33]. The turbulent wind tunnel environment in this study introduces additional variables, such as temperature and stress, to the SMA displacement modeling. This increases the complexity and reduces the accuracy of the estimation of SMA wire displacement. Moreover, incorporating SMA actuators into a flying object presents challenges related to weight and volume in the design process. Instead of sticking to conventional approaches, a lightweight and easy-to-implement SMA actuation mechanism is proposed.

The SMA actuator utilizes a uni-axial deflection arrangement similar to that of a servo. The SMA wire pulls the control surface up about a span-wise hinge line located near the trailing edge. To support the SMA wire, three 3D-printed parts were installed on each upper surface of the kite, as shown in Figure 6. The SMA wire passes through holes on part 1, 2 and 3, respectively. The two ends of the SMA wire were clamped to metal leads that were soldered to the positive and negative output pins of a PWM motor driver. The PWM signal sent from the flight computer triggers a current across the SMA wire, causing it to shrink due to joule heating and pull the control surface up. A rubber band was attached between the control surface and the wing on the lower surface to provide a restoring moment that brings the control surface back to its neutral position when the SMA wire is not activated. The hinge moment H required to deflect the test kite control surface can be estimated as [40],

$$H = qS_f c_f C_{H_\alpha} \alpha + qS_f c_f C_{H_\delta} \delta \quad (1)$$

where q is the dynamic pressure, S_f is the control surface reference area, C_f is the control surface reference chord and C_{H_α} and C_{H_δ} are the derivatives of the hinge moment coefficient with respect to the angle of attack (α) and the derivative of the hinge moment coefficient with respect to the control surface deflection (δ), respectively, estimated using DATCOM [3]. Table 2 is generated to estimate the required hinge moment at a 6.5 degree angle of attack for a 7 m/s wind speed. Based on the hinge moment estimation, a 200 µm diameter and 380 mm length titanium-rich nickel–titanium (NiTi) alloy was selected for the SMA actuator, as a trade off between output stress and cooling time.

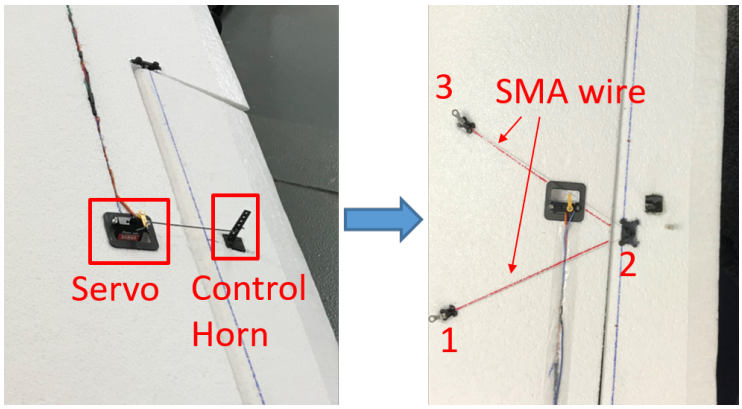

Figure 6. Control surface connection mechanism change.

Table 2. Hinge moment estimation for different control surface deflections (wind speed = 7 m/s).

Control Surface Deflection (deg)	Hinge Moment (Nm)
5	0.0113
10	0.0220
15	0.0300
20	0.0389
25	0.0473

Based on the SMA wire selection and installation mechanism, Table 3 tabulates the mass breakdown of the test kite's flight control systems actuated by SMA wire and an RC servo, respectively. Using the almost mass-less SMA wire saves weight in the mass budget compared to installing a servo motor. However, the higher power consumption of the SMA configuration requires a heavier battery. As a result, the overall weight of the SMA-based flight control system is almost equivalent to that of the baseline servo configuration.

Table 3. Servo and SMA actuator flight control system mass budget.

Servo Configuration		**SMA Configuration**	
Component	**Mass (g)**	**Component**	**Mass (g)**
Servo	12	SMA wire	1
2S battery	56	4S battery	63
Driver circuit	9	Driver circuit	2
Magnetic sensor	N/A	Magnetic Sensor	6
Total	77	Total	72

2.3. Kite Avionics and Flight Controller

Similar to the servo motor, a closed-loop feedback controller is introduced to the SMA actuator to enable precise control surface deflections. It is possible to estimate the SMA wire deformation based on the temperature change and stress applied using an empirical model (Figure 7). Then, the control surface deflections can be calculated from the deformation and trigonometry. Nonetheless, accurately estimating SMA shrinkage during a real flight is challenging because high-precision strain estimation systems are usually too heavy to be installed on an aircraft [25]. As an alternative, a linear magnetic sensor was installed to provide direct feedback of the spoiler deflection. Figure 8a illustrates the setup of the feedback sensor for deflection measurements. The magnets and hall sensors are fixed to the control surface and wing section, respectively. When the control surface is deflected, the magnetic reading from the hall sensor changes. The deflection angles are then calculated in real time, independent of varying ambient temperatures, aerodynamic loads and other external disturbances, using the predefined magnet-to-deflection mapping (Figure 8b).

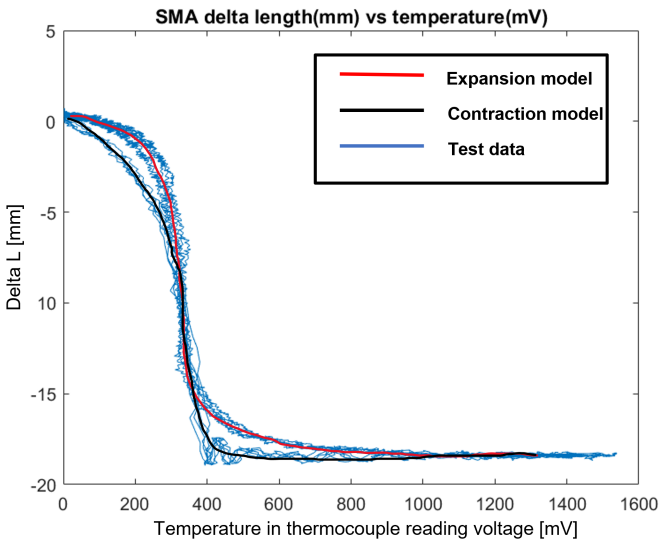

Figure 7. Shape memory effect of the 200 µm diameter SMA on the test kite. The temperature is in analog−digit converter units, mV. A higher mV represents a higher temperature.

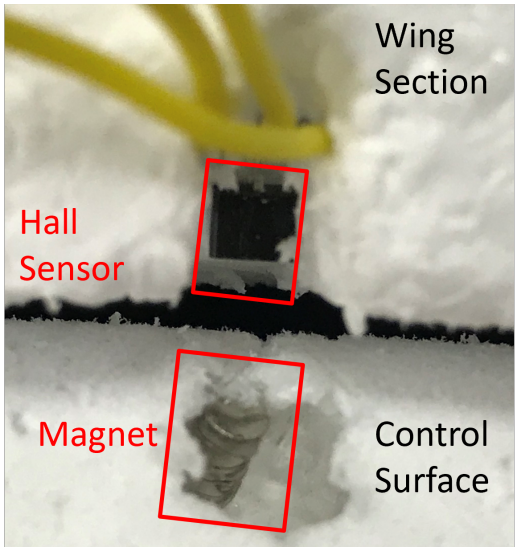

(**a**) Linear magnetic sensor installation.

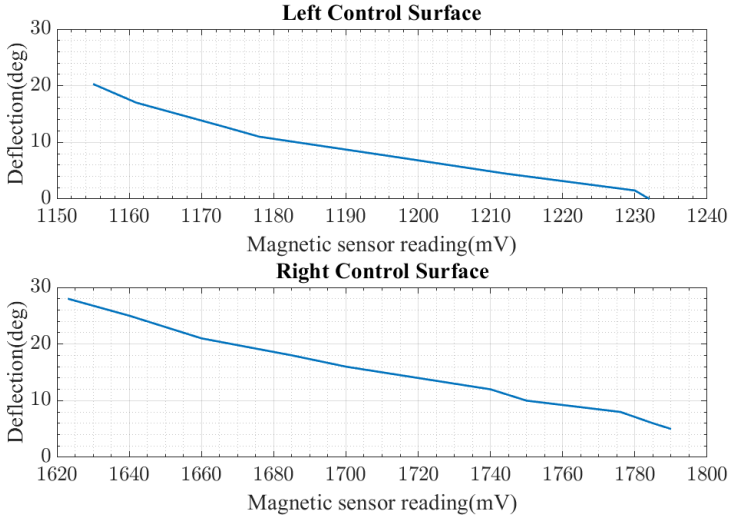

(**b**) SMA actuator magnetic reading to control surface deflection mapping.

Figure 8. The magnetic-sensor-based feedback mechanism of the SMA actuator.

In addition to the previously mentioned flight avionics, the Wit-Motion JY61 IMU (WitMotion Shenzhen Co.,Ltd, Shenzhen, China) was chosen for its cost-effectiveness, light weight and ability to provide acceleration, angular rates and Euler angles [41]. For the flight computer, the BeagleBone Blue Board (BeagleBoard.org, Michigan, USA) was selected due to its integration of commonly used buses and well-supported open-source libraries online [42], making the development of flight software more efficient.

Figure 9 depicts the complete set up of the flight control system for the SMA actuator bench test. The flight computer runs the flight code that generates desired control surface deflections based on IMU readings. Subsequently, the deflections are interpolated into PWM signals and transmitted to the PWM driver. The PWM driver adjusts the voltage across the SMA wire based on the duty cycle of the PWM signal, which deflects the control surface to the desired angle. The magnetic sensor measures the actual deflection and feeds back the magnitude of magnetism to the flight computer. Based on the error between the desired and feedback deflection angles, the computer generates a new PWM signal and the loop iterates.

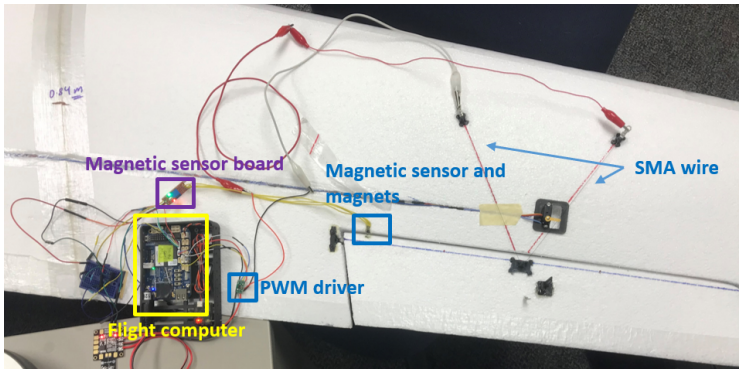

Figure 9. Test kite flight control avionics.

The flight software architecture, including a feedback control block diagram, is shown in Figure 10. The feedback controller consists of an outer loop for attitude control and an inner loop for SMA control. The error between desired and estimated Euler angles is input to the LQR/SISO outer loop, which yields the desired control surface deflection. The difference between the desired deflection and the angles estimated by the magnetic sensor is calculated. This difference is then fed into the PID inner loop, which outputs PWM duty cycles to switch voltage on and off across the SMA wire.

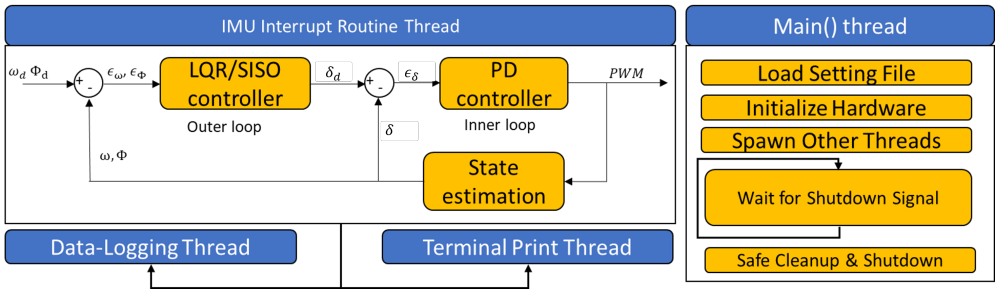

Figure 10. Complete kite flight software architecture.

Since BeagleBone Blue is a single processor board, pseudo-simultaneous multi-task calculation is realized using interrupt threads. After initializing the hardware, the main loop enters an infinite loop that waits for a terminating signal. Then, the IMU interrupt routine kicks in at a frequency of 200 Hz. In each IMU interrupt iteration, the kite states are estimated, and the control block diagram is executed as follows: The estimated kite angular rates (ω) and Euler angles (Φ) are compared with the desired kite angular rates (ω_d) and Euler angles (Φ_d). The state error for angular rates (ϵ_ω) and Euler angles (ϵ_Φ) is calculated and fed into the outer loop attitude controller. The LQR/SISO controller outputs a desired control surface deflection angle (δ_d), which is then compared with the estimated control surface deflection (δ). The error between the desired and estimated control surface deflection (ϵ_δ) is then fed into the inner loop SMA controller, which outputs a PWM signal to drive the SMA to the proper positions. Parallel to the IMU thread, a data-logging thread and a terminal print thread are executed at 10 Hz.

3. Iterative Design and Test of the SMA Actuator

With the SMA-to-deflection mechanism established, this chapter surveys paths to improve the SMA actuation algorithm and layout that fulfil the stability augmentation requirement. A few roadblocks were encountered during the subsequent actuator tests due to the intrinsic properties of the SMA wire. To maximize the control effectiveness, an iterative process of designing and testing the SMA actuator was conducted, involving trade-offs between actuation speed and power consumption.

3.1. Prototype SMA Actuator Tests and Improvements

Bench tests of the prototype SMA actuator shown in Figure 6 indicated that the SMA wire cannot respond as fast as a servo motor. Actuation delays were observed during the control surface moving up (SMA contraction) and moving down (SMA expansion) phases (Figure 11).

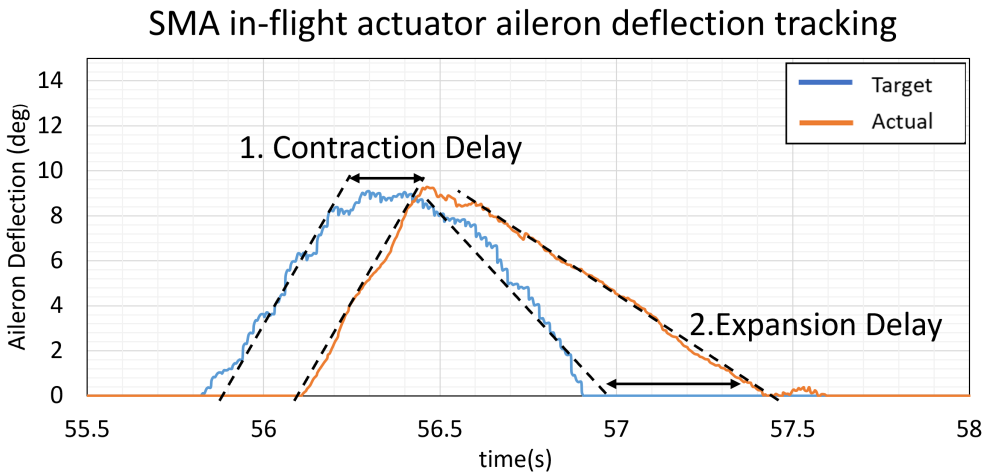

Figure 11. First SMA actuator flight test performance (a delay was observed at both the rising and falling phase).

The delay during the rising phase is caused by the time it takes for the SMA wire to heat up and initiate deformation, while the delay during the falling phase is caused by the time taken by the SMA wire to dissipate heat to the ambient. The contraction delay can be reduced by applying more Joule heat within a shorter time. Considering the SMA wire as a resistor with a fixed resistance value, increasing the voltage across the SMA wire boosts heating and minimizes the contraction delay. The actuation voltage was increased from 12 V to 16 V to achieve faster SMA actuation. The inner loop SMA controller gain was tuned accordingly to make sure that the SMA wire was not overheated.

Several countermeasures were also taken to reduce the expansion delay. It was observed that the expansion rate of the SMA wire decreases with its expansion, as the heat transfer rate decreases when the temperature gradient between the SMA wire and the ambient decreases. Therefore, the minimum spoiler deflection angle was reduced to 5°, so that the SMA wire would not enter the region of slow heat dissipation. In this application, the only way to transfer heat from the SMA wire is through passive cooling. Thus, it is crucial not to input excessive heat that could further delay the expansion of the SMA wire. The inner loop controller was modified to ensure that only the minimum energy required was input to the SMA wire. As soon as the SMA actuator overshoots, the controller cuts off the PWM output to prevent excessive heating of the SMA wire. Figure 12 shows the spoiler deflection performance of a bench test comparing the original and modified SMA controllers. It is evident that the expansion slope of the SMA actuator with the new controller was steeper, particularly when the deflection was above 5°.

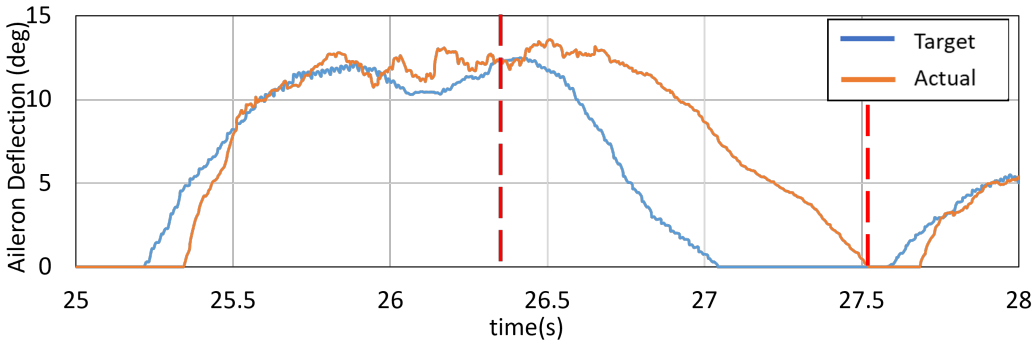

(**a**) Left spoiler deflection tracking.

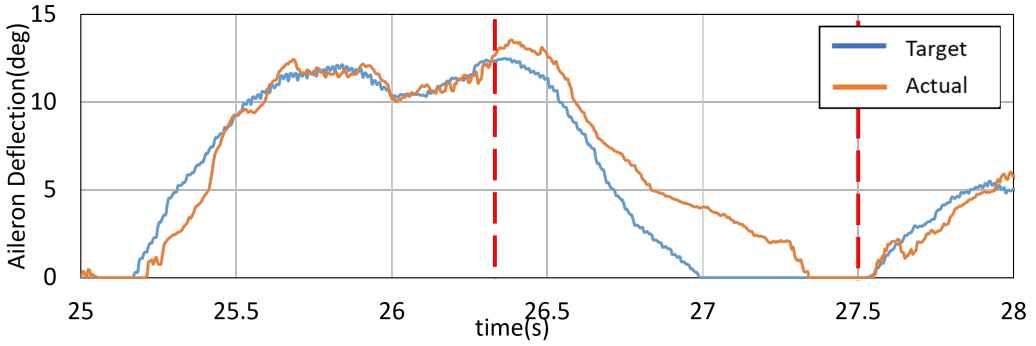

(**b**) Left spoiler deflection tracking with the modified SMA controller.

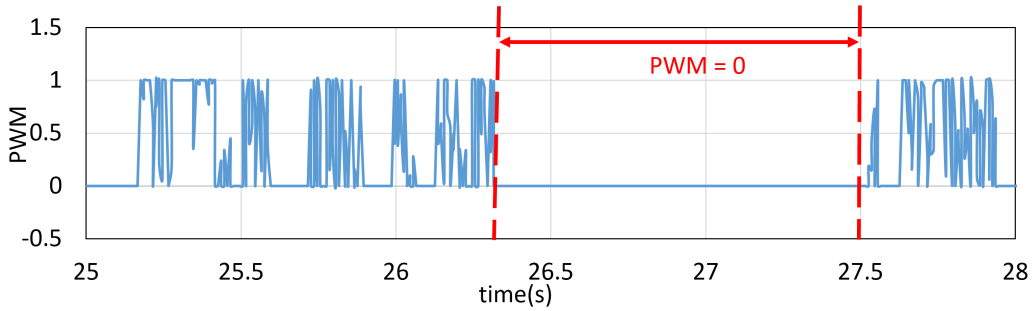

(**c**) PWM output of the modified SMA controller.

Figure 12. The modified controller improves the SMA actuator's cooling performance.

With the significant improvement in the response speed of the SMA actuator, the test kite was taken to a wind tunnel test. The deflection of the control surface was plotted in Figure 13. The rising delay of the control surface was noticeably reduced as the actuation voltage was increased to 16 V, in combination with the modified SMA controller. However, the falling delay was not significantly reduced by the modified controller, contrary to the expected reduced cooling time based on the bench test results shown in Figure 12. Since air cooling is the only method to dissipate the heat of the SMA wire, it is hypothesized that during actual wind tunnel tests, the high angle of attack of the kite caused flow separation towards the trailing edge, leading to an insufficient amount of cooling air passing through the SMA wire.

To test the hypothesis, bench tests were conducted to compare the SMA actuator's performance under different air cooling conditions. According to simulations in [3], the kite's trim angle of attack is around 12°. Therefore, the test kite was positioned at a 12° angle of attack and received air from a tower fan in front of the leading edge, as shown on the left side of Figure 14. This setup is intended to emulate real flight conditions. On the right side of Figure 14, cooling air was blown above the SMA wire. This setup provided

the maximum cooling effect to the SMA actuator and was also the configuration used to test the modified SMA actuator controller discussed in Figure 6. Figure 15 compares the spoiler deflection tracking between the two air cooling conditions. It was confirmed that the angle of attack hindered cooling air from circulating through the SMA wire, causing a high delay in SMA contraction.

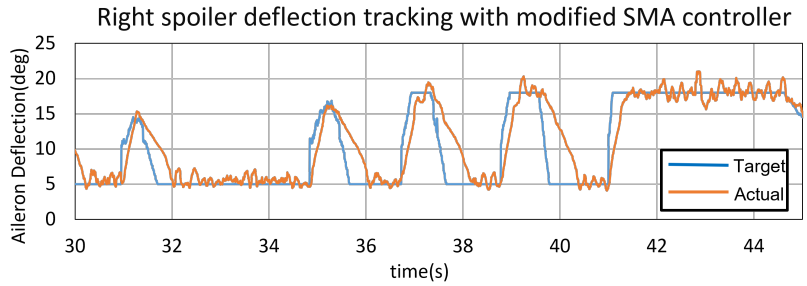

Figure 13. SMA actuator flight test performance with the modified SMA controller.

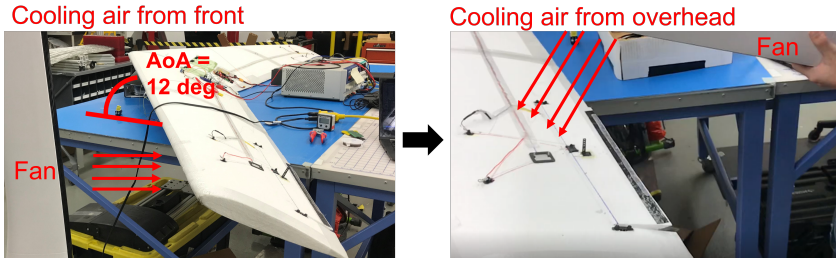

Figure 14. Test setup of SMA performance comparison under different cooling conditions. Parallel front wind cooling (on the **left**) versus overhead wind cooling (on the **right**).

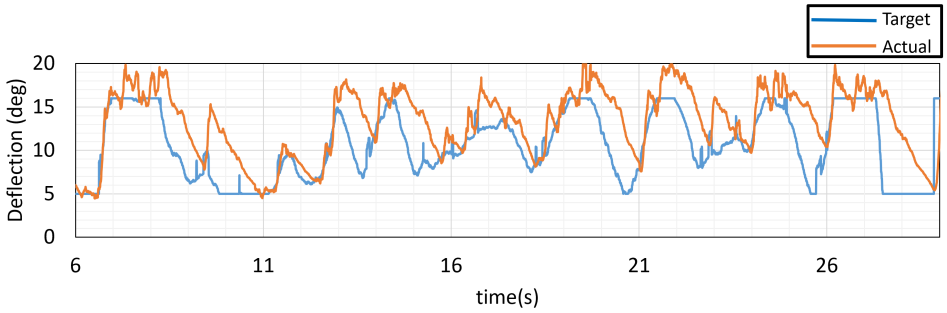

(**a**) Spoiler deflection tracking (cooling air from front).

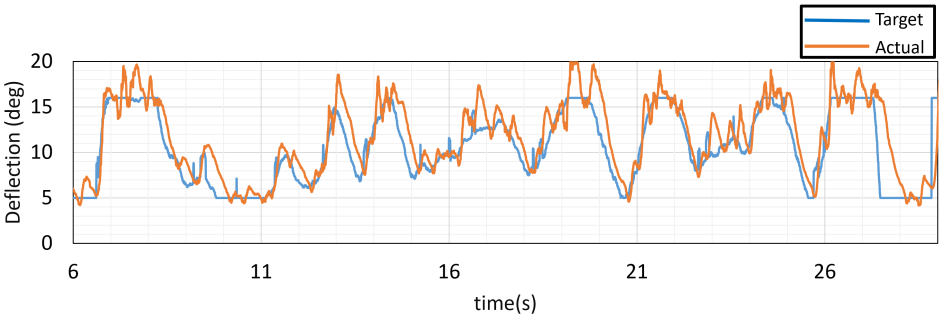

(**b**) Spoiler deflection tracking (cooling air from overhead).

Figure 15. Comparison of the prototype SMA actuator tracking under different cooling conditions.

3.2. New Layout SMA Actuator

As a countermeasure to allow sufficient cooling air to reach the SMA actuator at high angles of attack, a concept was introduced to move the SMA wire towards the leading edge (shown in Figure 16). Instead of directly pulling the control surface with the SMA wire,

the new SMA actuator design incorporates a transmission mechanism that converts the SMA wire's linear motion into the spoiler's angular motion using a connection wire. This new configuration exposes a larger segment of the SMA wire to the incoming air on the leading edge. Figure 17 displays a detailed view of the new layout SMA actuator. The SMA wire starts at Anchor 1, goes through the sliding block, turns around at Anchor 3, and finally returns to Anchor 1. The sliding block is connected to the control surface through a connection wire that is attached to Anchor 2. When voltage is applied, the sliding block is pulled forward due to SMA wire contraction, exerting tension on the connection wire to deflect the control surface. All three anchors are firmly mounted on the wing using epoxy.

Bench tests were conducted to evaluate the performance of the new layout SMA actuator. After converting the SMA actuator into the new configuration, the kite was positioned at two different angles of attack (Figure 18) and commanded to perform the same predefined deflection sequence that was utilized in the prototype SMA actuator bench tests shown in Figure 13. For the bench tests of the new layout SMA actuator, no significant differences were observed in the deflection tracking log. As shown in Figure 19, there is a slight degradation in the air cooling performance as the angle of attack increases, leading to a greater difference between the desired and actual deflection angles. By utilizing the same deflection command sequences in all bench tests, it becomes possible to compare the performance of the new layout SMA actuator with that of the old layout SMA actuator used in previous bench tests. Figure 20 demonstrates that even at higher angles of attack, the new layout SMA actuator exhibited a notably improved deflection tracking performance compared to the old design: (A) The new layout SMA actuator had less deflection overshooting. (B) The new layout SMA actuator allowed quicker cooling. (C) The retraction time from full deflection was significantly reduced. It was also observed that the performance of the new layout actuator at a 20 degree angle of attack was close to the performance of the prototype SMA actuator under optimal cooling conditions (overhead wind cooling conditions shown in Figure 14). The similar deflection tracking behavior indicates that the new actuator configuration may allow sufficient air to flow over the SMA wire during actual flight at high angles of attack.

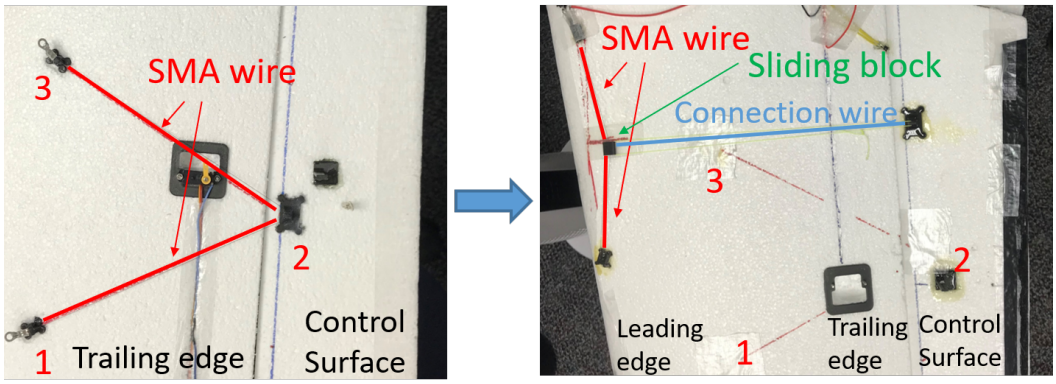

Figure 16. Comparison between old and new SMA actuator layout. In the old configuration (on the **left**), the SMA wire was fixed by 3D-printed parts 1, 2 and 3, numbered in red. In the new configuration (on the **right**), the SMA wire was relocated to the leading edge and a connection wire was used to pull the control surface.

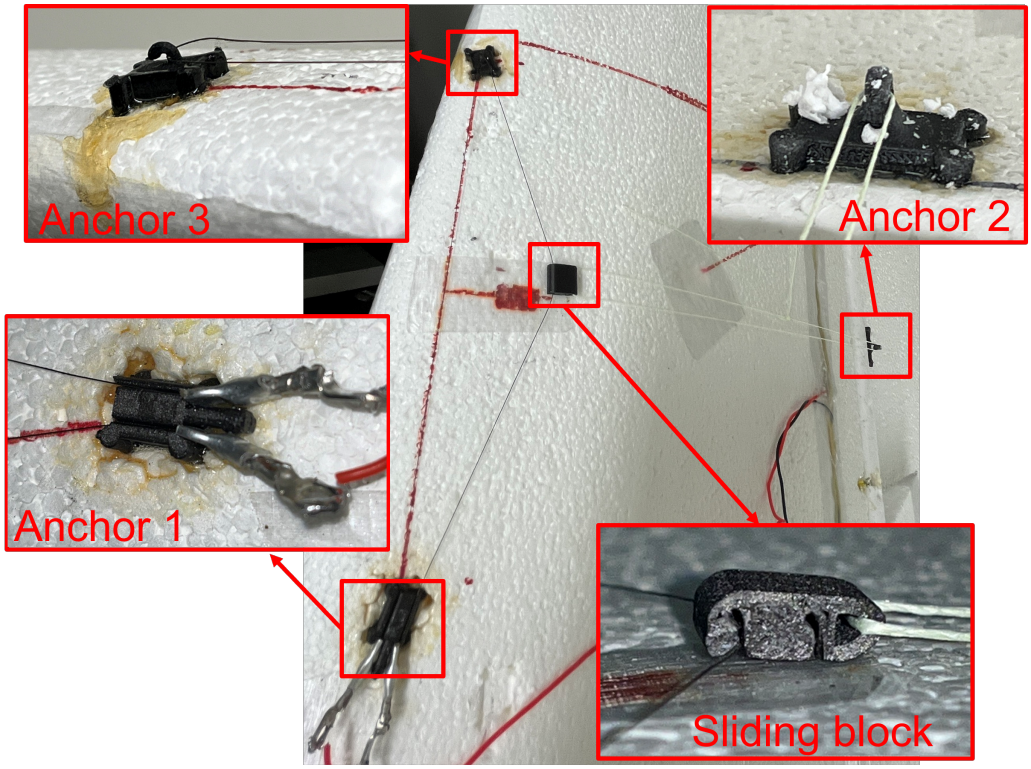

Figure 17. A detailed view of the new layout SMA actuator design and integration mechanism.

(**a**) Front wind cooling at a 12° angle of attack (**b**) Front wind cooling at a 20° angle of attack

Figure 18. Test setup of the new layout SMA actuator performance comparison under different cooling conditions.

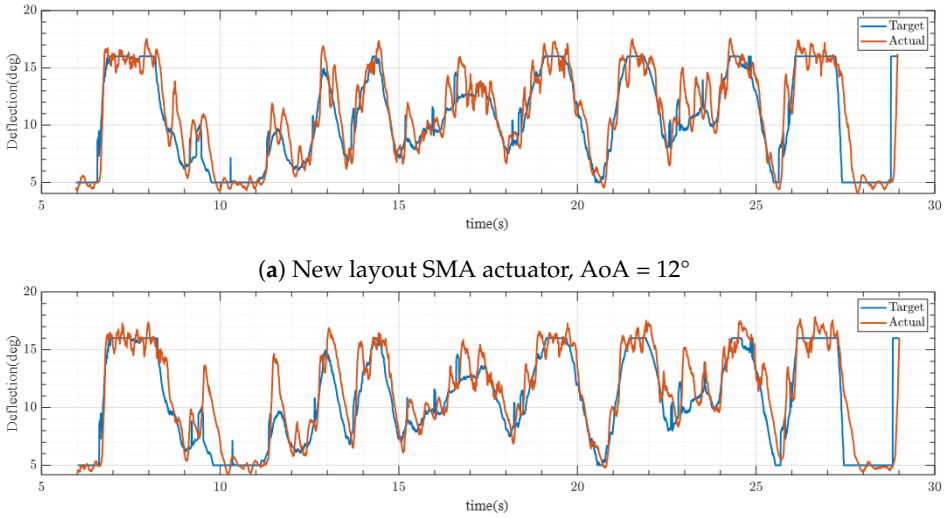

(**a**) New layout SMA actuator, AoA = 12°

(**b**) New layout SMA actuator, AoA = 20°

Figure 19. Comparison of new layout SMA actuator tracking under different angles of attack.

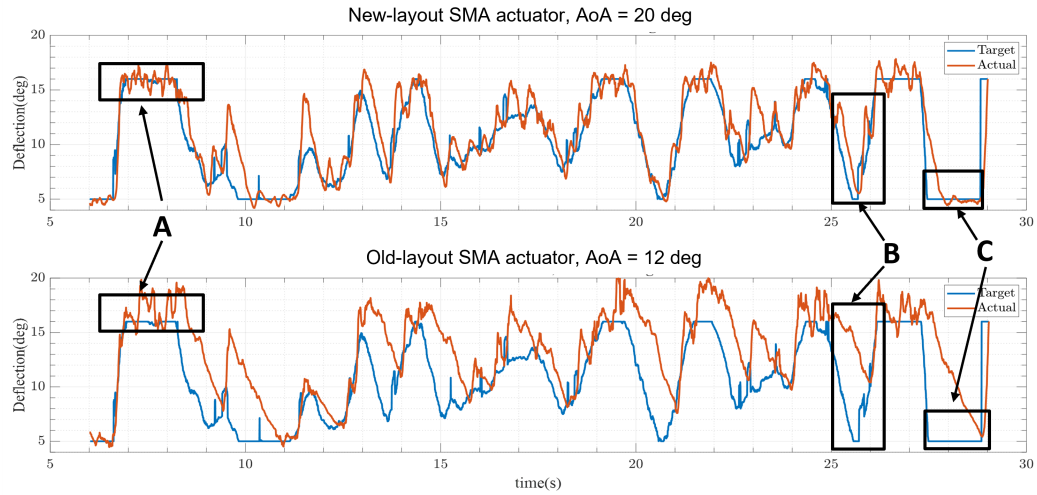

Figure 20. Comparison of old and new layout SMA actuators with the same deflection sequence under different cooling conditions. The results illustrate that **A**: the new layout SMA actuator has less deflection overshooting. **B**: The new layout SMA actuator has quicker cooling. **C**: The retraction time from full deflection is significantly reduced (from 1.3 s to 0.37 s).

3.3. New Layout SMA Actuator Incorporated Flight Dynamics Model

The improved performance of the new layout SMA actuator revealed its potential for achieving equilibrium flight. To evaluate the control system's capability, a numerical model was developed to simulate the motion of the test kite in steady flow. The linearized flight dynamics model of the test kite can be seen in Equation (2):

$$\begin{aligned} \dot{\boldsymbol{x}}(t) &= A\boldsymbol{x}(t) + B\boldsymbol{u}(t) \\ \boldsymbol{y}(t) &= C\boldsymbol{x}(t) + D\boldsymbol{u}(t) \end{aligned} \tag{2}$$

where A, B, C, D are the state space matrices linearized about the kite equilibrium point. A detailed numerical derivation of the state space model can be found in [3]. The state space vector $\boldsymbol{x}$(t) and input vector $\boldsymbol{u}$(t) are:

$$\boldsymbol{x}(t)^T = \begin{bmatrix} K & \Psi & \theta & \psi & \phi & \dot{K} & \dot{\Psi} & \dot{\theta} & \dot{\psi} & \dot{\phi} \end{bmatrix} \tag{3}$$

$$\boldsymbol{u}(t) = [\delta] \tag{4}$$

where K is the kite elevation, Ψ is the kite azimuth and θ, ψ and ϕ are the kite pitch, yaw and roll angle, respectively. The aileron deflection angle is denoted as δ in the input vector.

The control input, i.e., the spoiler deflection, was produced by servo motors in [3]. The actuation delay was ignored in the original flight dynamics model since the servos respond almost instantaneously. However, substituting servo motors with SMA actuators required the model of the actuator to emulate the control surface dynamics. The SMA actuator exhibits distinctive contraction and expansion dynamics due to the hysteresis effect (Figure 11). Thus, the deflection dynamics of the spoiler moving up and down were modeled separately. Grigorie et al. [43] proposed an approach that utilizes the Matlab System Identification Toolbox to generate SMA actuation transfer functions from its step response results, without involving complex analytical formulations of SMA dynamics. Employing the System ID Toolbox and the new layout SMA actuator bench test results shown in Figure 20, an empirical model of SMA actuator dynamics was proposed (Figure 21):

$$H_c(s) = \frac{-3.761s + 167.4}{s^2 + 12.44s + 173.7} \tag{5}$$

$$H_e(s) = \frac{245.4s^2 + 1806s + 29200}{s^3 + 281.4s^2 + 2229s + 17710} \tag{6}$$

where the transfer function input is the target spoiler deflection. Furthermore, the output is the actual spoiler deflection. $H_c(s)$ and $H_e(s)$ are the transfer functions for SMA contraction and expansion phases, respectively. Since the SMA wire expansion purely relies on natural cooling, the cooling dynamics model is commonly obtained from the distinctive thermal condition of SMA application. In addition, to avoid the complexity of switching between contraction and expansion curves, merely the rising dynamics are included for SMA controller development [43–45]. Applying the same methodology, only the heating transfer function $H_c(s)$ was considered to prescribe spoiler deflections in the kite dynamics model for flight controller design. Figure 22 illustrates the attainment of a stable root locus for the kite flight dynamics with the implementation of an LQR controller.

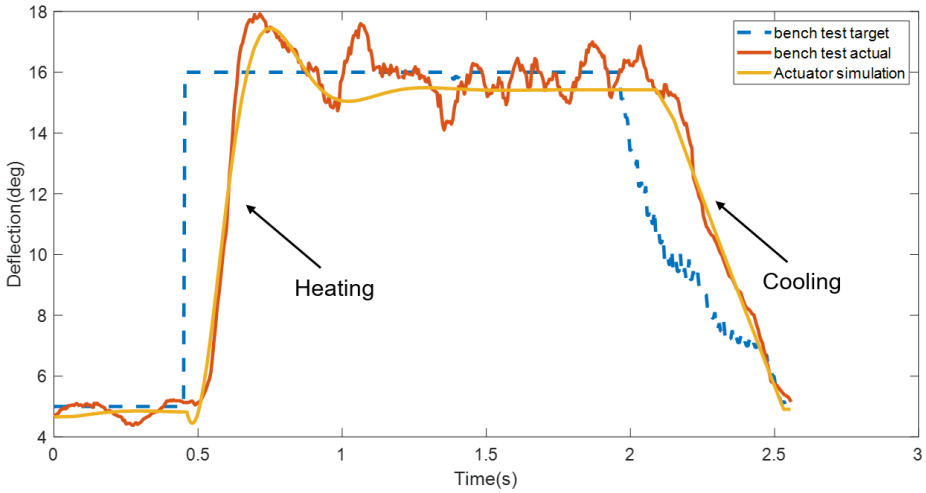

Figure 21. Simulated spoiler deflection step response versus time for bench test results.

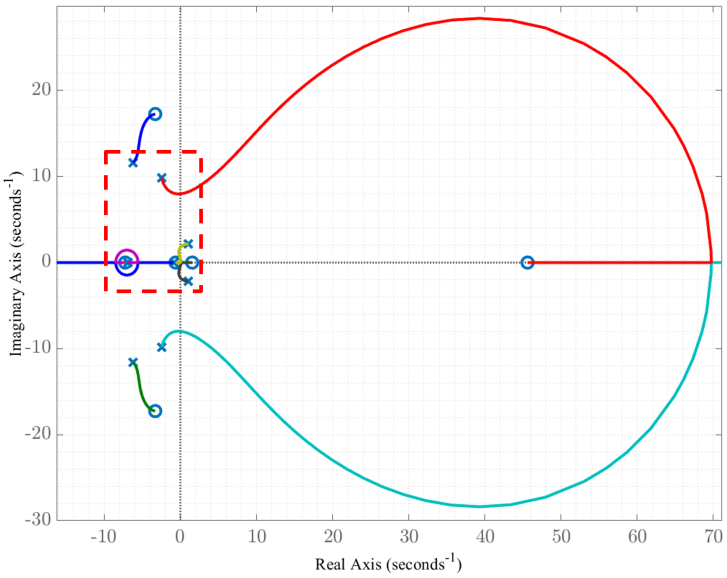

(**a**) Root locus of longitudinal kite flight dynamics with an LQR controller.

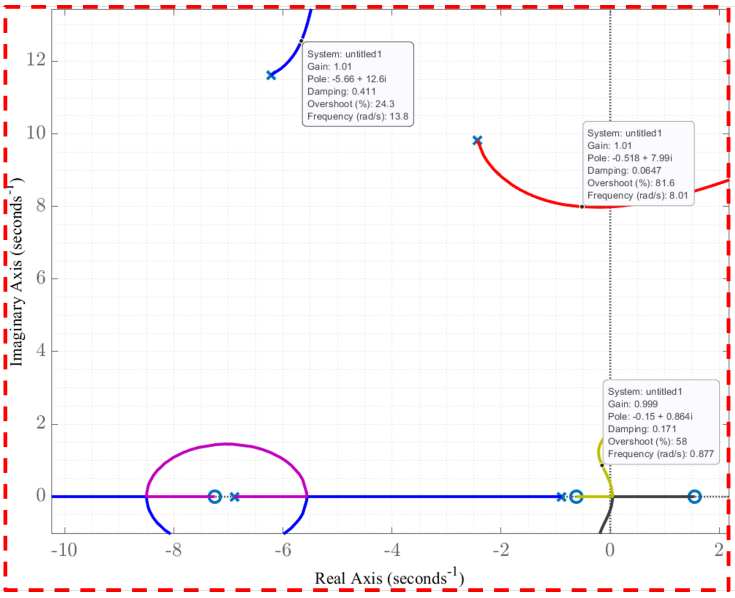

(**b**) Behavior of poles near the origin on root locus.

Figure 22. The root locus plot indicates that stable flight can be achieved by the LQR controller.

Even though only the SMA actuator heating transfer function was involved in the controller design, both the SMA actuator heating and cooling dynamics were included in the kite flight dynamics simulation to evaluate the flight controller's effectiveness. A Simulink model, shown in Figure 23, was established for stability augmentation verification. The input variables of the model are the lateral attitudes and angular rates at trim flight:

$$\boldsymbol{x_d} = \begin{bmatrix} \psi_d \\ \dot{\psi}_d \\ \phi_d \\ \dot{\phi}_d \end{bmatrix} = \begin{bmatrix} 0 \\ 0 \\ 0 \\ 0 \end{bmatrix}$$

To observe the LQR controller effectiveness, an initial disturbance was introduced to the dynamics model:

$$\begin{aligned} \boldsymbol{x}(t_0)^T &= \begin{bmatrix} K & \Psi & \theta & \psi & \phi & \dot{K} & \dot{\Psi} & \dot{\theta} & \dot{\psi} & \dot{\phi} \end{bmatrix} \\ &= \begin{bmatrix} 0 & 0 & \frac{\pi}{6} & -\frac{\pi}{18} & \frac{\pi}{18} & 0 & 0 & 0 & 0.1 & -0.1 \end{bmatrix} \end{aligned} \tag{7}$$

where the initial condition of the first five states is given in radians (rad) and the remaining states are given in radians per second (rad/s). As shown in Figure 24, the lateral attitudes and angular rates of the kite started from a disturbed status but eventually recovered to equilibrium flight. Figure 25 displays the time history of control surface deflection. Although there was a delay in the contraction and expansion of the SMA, it was able to briefly track the desired control surface deflection. The simulation results demonstrate that the SMA-based stability augmentation system, when combined with the LQR controller, is capable of fulfilling the stability augmentation requirement.

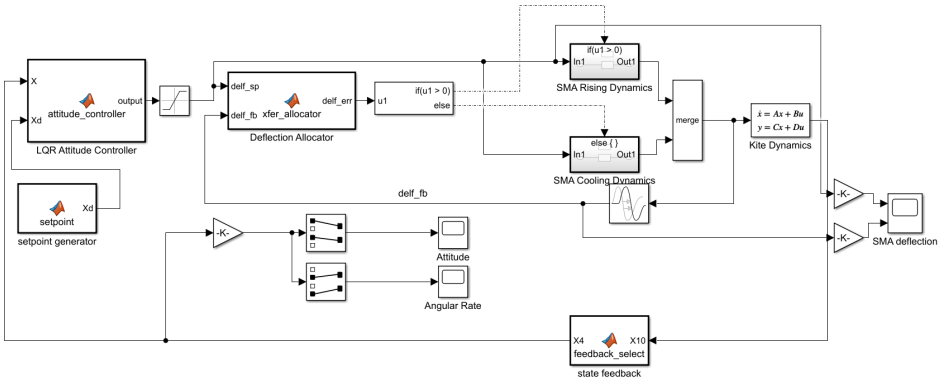

Figure 23. Dynamic model of the test kite with the new layout SMA actuator.

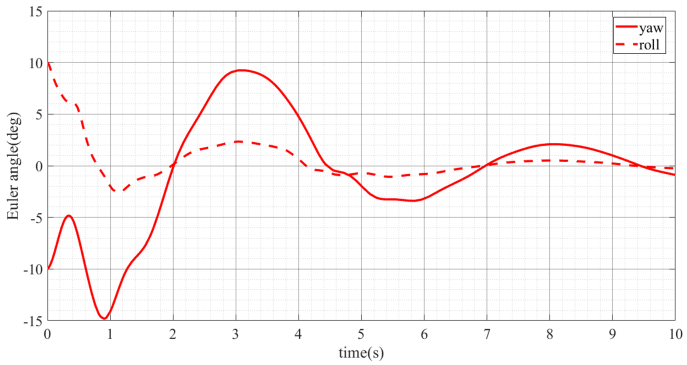

(**a**) Yaw and roll angle.

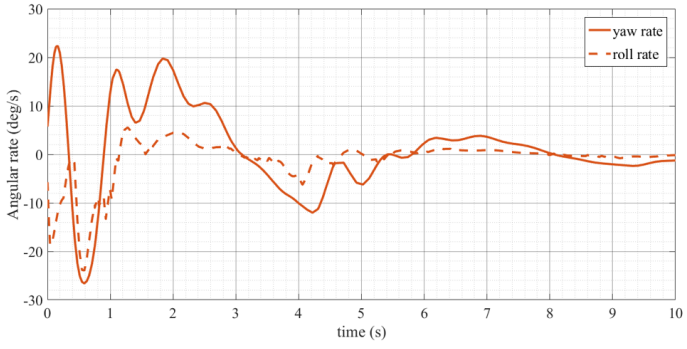

(**b**) Yaw rate and roll rate.

Figure 24. Simulated lateral step input response of the test kite with the SMA-based stability augmentation system.

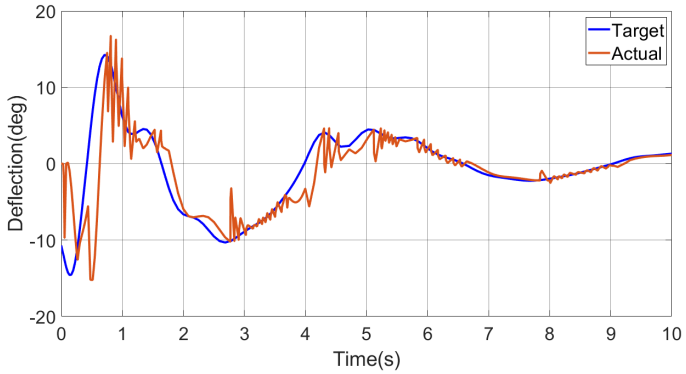

Figure 25. Simulated SMA-actuated spoiler step input response (a positive deflection represents the right spoiler is open and vice versa).

3.4. Flight Test with the New Layout SMA Actuator

Following the demonstration of the capability to recovery from perturbations in simulation, the SMA actuators were installed on the proof of concept kite for wind tunnel test verification. Stable flight was successfully achieved by the new layout SMA actuator with deflection angles outputted by the LQR attitude controller (Figure 26).

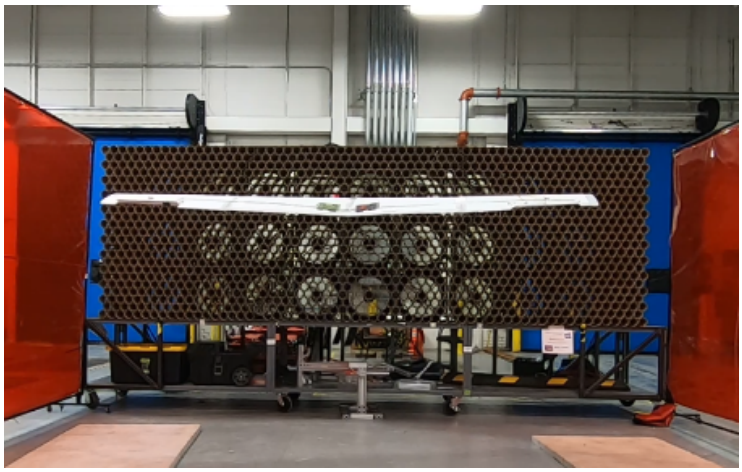

Figure 26. Stable flight achieved during wind tunnel test.

Flight data were afterwards collected from the flight computer and plotted in Figure 27. The top plot shows the time history of the kite's Euler angles. The roll and yaw angles continuously oscillated around zero, implying steady flight in the presence of disturbance. By subtracting the IMU installation angle, an average angle of attack of 15° was obtained, which agrees with the angle of attack predicted by simulation [3]. The bottom two plots show the time history of spoiler deflections generated by each SMA actuator. The setpoint deflections were essentially followed by actual ones, with small steady tracking errors fluctuating around them. It is notable that the tracking errors are mostly negative. This is because the cooling effect in wind tunnel tests is much greater than in a bench test. In bench tests, a 4 m/s airflow was produced by a tower fan on each side of the wing to dissipate heat from SMA wire, whereas in wind tunnel tests, a matrix of heavy-duty fans blew a 7 m/s airflow towards the SMA actuators. With considerable heat loss over time, the SMA wires could not reach the desired shrinkage in time, yielding small state errors. Figure 28 further substantiates this inference by investigating the PWM signal sent to the voltage driver. Between approximately 58.3 and 58.8 s, the PWM was 100%, which guaranteed the quickest energizing to contract the SMA wire. A negative state error was still observed on the deflection curve, indicating that the SMA wire demanded more heat input even though it was at its maximum power output level. On the other hand, the SMA wire's expansion

behavior benefited from the strong air cooling effect in the wind tunnel. The cooling delay was reduced to 0.13 s, which is comparable to the servo motor's 0.1 s actuation delay.

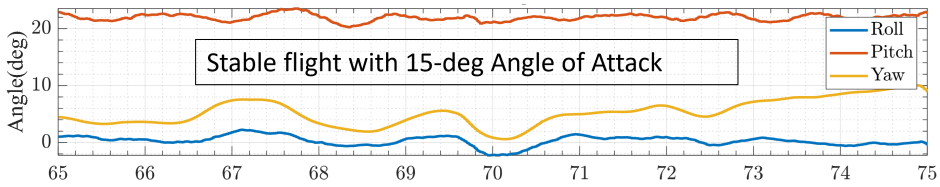

(**a**) Test kite Euler angle.

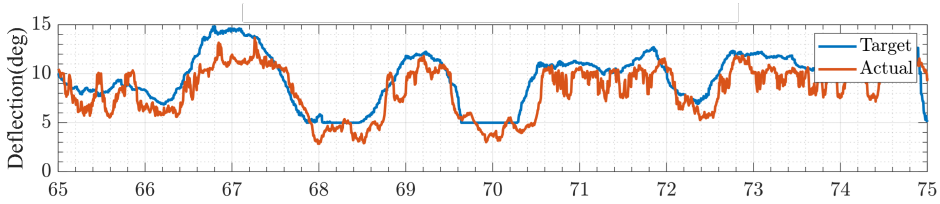

(**b**) New layout SMA actuated spoiler deflection tracking (left wing).

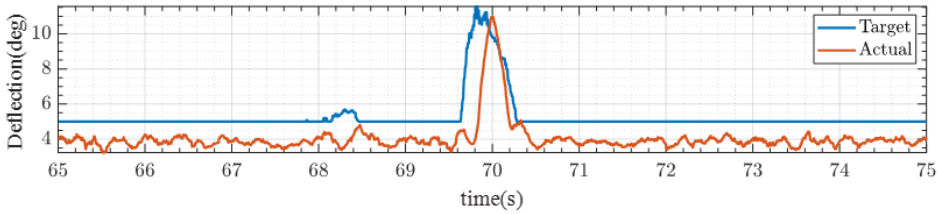

(**c**) New layout SMA actuated spoiler deflection tracking (right wing).

Figure 27. Flight test performance with the new layout SMA actuator. The spoiler rise was delayed because of the excessive cooling in the wind.

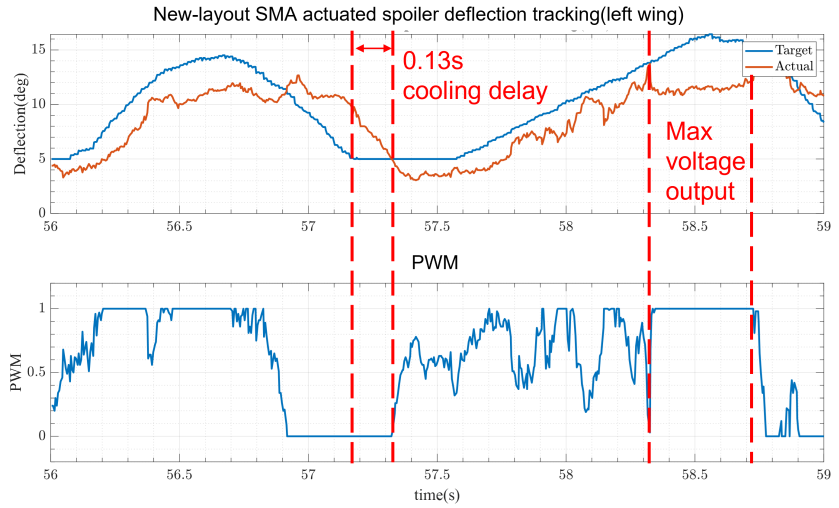

Figure 28. Flight log of the new layout SMA actuator (left) deflection and PWM output. The faster cooling in the wind tunnel resulted in the SMA wire being under-actuated, leading to a negative tracking error for spoiler deflection.

The wind tunnel test verified that the new layout SMA actuator can achieve a response time comparable to a servo motor when adequately cooled. However, this comes at the cost of an increased actuation delay for the SMA actuator. Additionally, it would be challenging to reach desired deflections due to inadequate heat input. Due to the absence of a high-fidelity SMA displacement model and more sophisticated control laws, the proposed SMA actuator could not achieve high-precision spoiler deflections compared to an RC servo. A

weight estimation of the control system for long-endurance flights was performed. The power consumption was measured and extended for a 24 h flight. The SMA configuration consumes more energy than the servo configuration as anticipated, leading to a larger battery and a higher system weight (Figure 29). However, a much higher actuation stress is available from the SMA wire.

In conclusion, specific conditions need to be fulfilled for SMA actuators to achieve a servo-motor-level actuation performance and accuracy. Nonetheless, the wind tunnel test results demonstrated that even though the SMA actuator did not operate under perfect conditions, the deflection uncertainty was found to be small enough to be covered by a robust attitude controller. Furthermore, one possible solution to compensate for the heat deficiency is to apply a higher voltage across the SMA wire so that more energy is supplied. A voltage-adjustable power supply is preferred so that the maximum voltage applied to the SMA wire can be changed in real time according to the ambient cooling conditions.

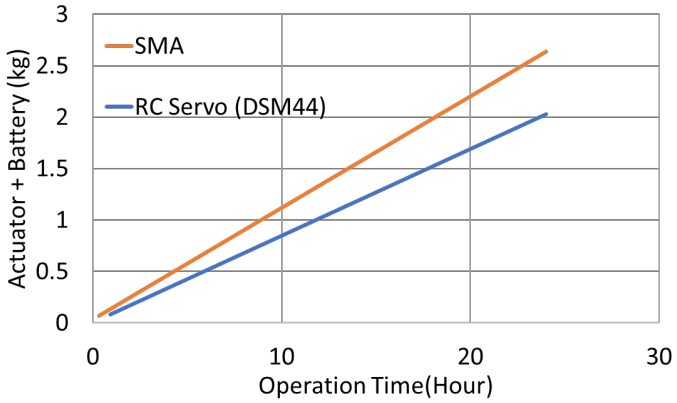

Figure 29. Long-endurance flight control system weight comparison.

4. Conclusions and Future Work

This paper presents the iterative process of developing an SMA-wire-based flight control actuator for inflatable structures. Compared with traditional electromagnetic servos, the SMA actuator is investigated for its outstanding force-to-mass ratio and mechanical compatibility with inflatable structures. After conducting flight tests on the proof-of-concept kite in a wind tunnel, it was observed that:

1. The improved SMA actuators, controlled by an in-house developed attitude controller, successfully stabilized the kite in the presence of turbulent wind.
2. The SMA actuator's responsiveness and accuracy are comparable to a servo motor. However, because of the SMA actuator's sensitivity to ambient cooling conditions, it is rather challenging to always achieve such quick and precise deflections.

Unstable cooling behavior is the major bottleneck for SMAs to achieve high-speed actuation. Unless a breakthrough in technology takes place in the SMA field to simplify modeling or to increase the actuation accuracy, it is more preferred to utilize SMA actuator for movements that require lower frequency operations. SMA actuators are more suitable for actuating slats, flaps or other control surfaces for lift augmentation, airfoil morphing and heading control purposes. For example, NASA has successfully applied an SMA to fold wings to different angles while in the air [46]. Moreover, SMA actuators may also be utilized for actuation that only takes place during taking off and landing phases that happen once per flight.

In future work, the SMA actuator mechanism will be further improved, for example, resistance feedback modeling shall be introduced into the control scheme [31]. Precise control surface deflections may be achieved by incorporating resistance-based feedback control with a Kalman filter [33]. Thermal pads and fans may be considered to accelerate SMA cooling; however, installing additional components overshadows SMA's low-weight advantage. Jeong et al. have proposed a coolant-vessel-based SMA actuator, aiming to

achieve a balance between cooling performance and structural complexity [47]. SMA cooling phase dynamics may also be considered in controller design to achieve optimal controller tuning.

Author Contributions: Conceptualization, R.T., T.N. and Y.Z.; methodology, R.T. and Y.Z.; software, formal analysis, investigation, Y.Z.; simulation, validation, Y.Z. and R.G.; draft manuscript preparation, Y.Z. and R.G.; supervision, T.N. All authors have read and agreed to the published version of the manuscript.

Funding: This research received no external funding .

Data Availability Statement: Data available on request from the authors.

Acknowledgments: The authors would like to thank Azwan Aris, Eric Smith and Mark Smith (Toyota Research Institute North America) for building the wind tunnel in Figure 4 and assisting with the wind tunnel tests.

Conflicts of Interest: The authors declare no conflicts of interest.

References

1. Itakura, E. Save from Future Japan Social Crises! "Mothership" Project. In Proceedings of the Airborne Wind Energy Conference 2019, Glasgow, Scotland, 15–16 October 2019.
2. Nam, T.; Vahid, O.; Gupta, R.; Kapania, R.K. High Altitude Airborne Wind Energy. In Proceedings of the AIAA Scitech 2021 Forum, Virtual Event, 11–15 January 2021; p. 1815.
3. Gupta, R.; Zhu, Y.; Nam, T. Flight Dynamics, Control Law Design, and Flight Tests of Kite. In Proceedings of the AIAA AVIATION 2021 FORUM, Virtual Event, 2–6 August 2021; p. 2462.
4. Zhu, Y.; Gupta, R.; Aris, A.; Nam, T. Development and Testing of the Flight Control System for a Tethered Wing. In Proceedings of the AIAA Scitech 2022 Forum, San Diego, CA, USA, 3–7 January 2022; p. 2049.
5. Gupta, R.; Zhu, Y.; Nam, T.; Tsukada, T.; Fukagawa, T.; Itakura, E. Cross Wind Flight Dynamics Modeling of Tethered Kite. In Proceedings of the AIAA Scitech 2022 Forum, San Diego, CA, USA, 3–7 January 2022; p. 0136.
6. Woods, B.K.; Fincham, J.H.; Friswell, M.I. Aerodynamic modelling of the fish bone active camber morphing concept. In Proceedings of the RAeS Applied Aerodynamics Conference, Bristol, UK, 22–24 July 2014; Volume 2224.
7. Rivero, A.E.; Weaver, P.M.; Cooper, J.E.; Woods, B.K. Parametric structural modelling of fish bone active camber morphing aerofoils. *J. Intell. Mater. Syst. Struct.* **2018**, *29*, 2008–2026. [CrossRef]
8. Meguid, S.; Su, Y.; Wang, Y. Complete morphing wing design using flexible-rib system. *Int. J. Mech. Mater. Des.* **2017**, *13*, 159–171. [CrossRef]
9. Zekry, D.A.; Nam, T.; Gupta, R.; Zhu, Y.; Wissa, A.A. Covert-inspired flaps: An experimental study to understand the interactions between upperwing and underwing covert feathers. *Bioinspir. Biomimetics* **2023**, *18*, 046021. [CrossRef]
10. Tang, Y.; Qin, L.; Li, X.; Chew, C.M.; Zhu, J. A frog-inspired swimming robot based on dielectric elastomer actuators. In Proceedings of the 2017 IEEE/RSJ International Conference on Intelligent Robots and Systems (IROS), Vancouver, BC, Canada, 24–28 September 2017; IEEE: Piscataway Township, NJ, USA, 2017; pp. 2403–2408.
11. Lin, P.W.; Liu, C.H. Bio-inspired soft proboscis actuator driven by dielectric elastomer fluid transducers. *Polymers* **2019**, *11*, 142. [CrossRef] [PubMed]
12. Tang, Y.; Chi, Y.; Sun, J.; Huang, T.H.; Maghsoudi, O.H.; Spence, A.; Zhao, J.; Su, H.; Yin, J. Leveraging elastic instabilities for amplified performance: Spine-inspired high-speed and high-force soft robots. *Sci. Adv.* **2020**, *6*, eaaz6912. [CrossRef] [PubMed]
13. Ricotti, L.; Trimmer, B.; Feinberg, A.W.; Raman, R.; Parker, K.K.; Bashir, R.; Sitti, M.; Martel, S.; Dario, P.; Menciassi, A. Biohybrid actuators for robotics: A review of devices actuated by living cells. *Sci. Robot.* **2017**, *2*, eaaq0495. [CrossRef] [PubMed]
14. Liang, W.; Liu, H.; Wang, K.; Qian, Z.; Ren, L.; Ren, L. Comparative study of robotic artificial actuators and biological muscle. *Adv. Mech. Eng.* **2020**, *12*, 1687814020933409. [CrossRef]
15. Guo, Y.; Liu, L.; Liu, Y.; Leng, J. Review of dielectric elastomer actuators and their applications in soft robots. *Adv. Intell. Syst.* **2021**, *3*, 2000282. [CrossRef]
16. Rich, S.I.; Wood, R.J.; Majidi, C. Untethered soft robotics. *Nat. Electron.* **2018**, *1*, 102–112. [CrossRef]
17. Pololu. Power HD High-Speed Digital Micro Servo DSM44. 2023. Available online: https://www.pololu.com/product/2142 (accessed on 27 February 2023).
18. Fichera, S.; Isnardi, I.; Mottershead, J.E. High-bandwidth morphing actuator for aeroelastic model control. *Aerospace* **2019**, *6*, 13. [CrossRef]
19. Hunter, I.W.; Hollerbach, J.M.; Ballantyne, J. A comparative analysis of actuator technologies for robotics. *Robot. Rev.* **1991**, *2*, 299–342.
20. Kota, S.; Hetrick, J.A.; Osborn, R.; Paul, D.; Pendleton, E.; Flick, P.; Tilmann, C. Design and application of compliant mechanisms for morphing aircraft structures. In *Smart Structures and Materials 2003: Industrial and Commercial Applications of Smart Structures Technologies*; SPIE: Bellingham, DC, USA, 2003; Volume 5054, pp. 24–33.

21. Shintake, J.; Rosset, S.; Schubert, B.; Floreano, D.; Shea, H. UAVs Flex Their Artificial Muscles. 2021. Available online: https://spectrum.ieee.org/uavs-flex-their-artificial-muscles (accessed on 27 February 2023).
22. Kim, J.; Kim, J.W.; Kim, H.C.; Zhai, L.; Ko, H.U.; Muthoka, R.M. Review of soft actuator materials. *Int. J. Precis. Eng. Manuf.* **2019**, *20*, 2221–2241. [CrossRef]
23. Plante, J.S.; Dubowsky, S. Large-scale failure modes of dielectric elastomer actuators. *Int. J. Solids Struct.* **2006**, *43*, 7727–7751. [CrossRef]
24. Citro, M.; Coco, S. Fatigue behavior of Shape Memory Alloy wires actuated at high speed. In Proceedings of the ACTUATOR 2022, International Conference and Exhibition on New Actuator Systems and Applications, Mannheim, Germany, 28–30 June 2022; VDE: Frankfurt am Main, Germany, 2022; pp. 1–4.
25. Motzki, P.; Gorges, T.; Kappel, M.; Schmidt, M.; Rizzello, G.; Seelecke, S. High-speed and high-efficiency shape memory alloy actuation. *Smart Mater. Struct.* **2018**, *27*, 075047. [CrossRef]
26. Mabe, J.H.; Calkins, F.T.; Ruggeri, R.T. Full-scale flight tests of aircraft morphing structures using SMA actuators. In Proceedings of the Active and Passive Smart Structures and Integrated Systems 2007, San Diego, CA, USA, 19–22 March 2007; International Society for Optics and Photonics: Bellingham, DC, USA, 2007; Volume 6525, p. 65251C.
27. Calkins, F.T.; Mabe, J.H. Shape Memory Alloy Based Morphing Aerostructures. *J. Mech. Des.* **2010**, *132*, 111012. [CrossRef]
28. Yuchen, C.; Xing, S.; Jiefeng, L.; Jinjin, C. Nonlinear hysteresis identification and compensation based on the discrete Preisach model of an aircraft morphing wing device manipulated by an SMA actuator. *Chin. J. Aeronaut.* **2019**, *32*, 1040–1050.
29. Simpson, A.; Jacob, J.; Smith, S. Flight control of a UAV with inflatable wings with wing warping. In Proceedings of the 24th AIAA Applied Aerodynamics Conference, San Francisco, CA, USA, 5–8 June 2006; p. 2831.
30. Brennison, M.; Barrett, R.; Kerth, L. Development and flight test of a shape memory alloy actuator flight control system. In *Active and Passive Smart Structures and Integrated Systems 2010*; SPIE: Bellingham, DC, USA, 2010; Volume 7643, pp. 887–900.
31. Song, H.; Kubica, E.; Gorbet, R. Resistance modelling of SMA wire actuators. In Proceedings of the International Workshop on Smart Materials, Structures & NDT in Aerospace Conference, Montreal, QC, Canada, 2–4 November 2011.
32. Courtney, T.H. *Mechanical Behavior of Materials*; Waveland Pr Inc.: Boston, MA, USA, 2005.
33. Zhang, D.; Zhao, X.; Han, J.; Li, X.; Zhang, B. Active modeling and control for shape memory alloy actuators. *IEEE Access* **2019**, *7*, 162549–162558. [CrossRef]
34. Sayyaadi, H.; Zakerzadeh, M.R. Position control of shape memory alloy actuator based on the generalized Prandtl–Ishlinskii inverse model. *Mechatronics* **2012**, *22*, 945–957. [CrossRef]
35. Jayender, J.; Patel, R.V.; Nikumb, S.; Ostojic, M. Modeling and control of shape memory alloy actuators. *IEEE Trans. Control. Syst. Technol.* **2008**, *16*, 279–287. [CrossRef]
36. Hannen, J.C.; Crews, J.H.; Buckner, G.D. Indirect intelligent sliding mode control of a shape memory alloy actuated flexible beam using hysteretic recurrent neural networks. *Smart Mater. Struct.* **2012**, *21*, 085015. [CrossRef]
37. Kha, N.B.; Ahn, K.K. Position control of shape memory alloy actuators by using self tuning fuzzy PID controller. In Proceedings of the 2006 1ST IEEE Conference on Industrial Electronics and Applications, Singapore, 24–26 May 2006; IEEE: Piscataway Township, NJ, USA, 2006; pp. 1–5.
38. Nakshatharan, S.S.; Dhanalakshmi, K.; Ruth, D.J.S. Fuzzy based sliding surface for shape memory alloy wire actuated classical super-articulated control system. *Appl. Soft Comput.* **2015**, *32*, 580–589. [CrossRef]
39. Nikdel, N.; Nikdel, P.; Badamchizadeh, M.A.; Hassanzadeh, I. Using neural network model predictive control for controlling shape memory alloy-based manipulator. *IEEE Trans. Ind. Electron.* **2013**, *61*, 1394–1401. [CrossRef]
40. Etkin, B.; Reid, L.D. *Dynamics of Flight: Stability and Control*; John Wiley & Sons: Hoboken, NJ, USA, 1995.
41. WITMOTION. WT61P. 2022. Available online: https://www.wit-motion.com/6-axis/witmotion-wt61-6-axis-ahrs-sensor-digital.html (accessed on 27 February 2023).
42. Nelson, R.; Yoder, M.; Lechner, D.; Casner, D.; Agar, D.; Govostes, R. *Librobotcontrol, Software Package*, Version 1.0. 2015. Available online: https://github.com/beagleboard/librobotcontrol (accessed on 24 February 2022).
43. Grigorie, T.L.; Popov, A.V.; Botez, R.M.; Mamou, M.; Mébarki, Y. A Morphing Wing used Shape Memory Alloy Actuators New Control Technique with Bi-positional and PI Laws Optimum Combination—Part 1: Design Phase. In Proceedings of the ICINCO, Funchal, Portugal, 15–18 June 2010.
44. Liu, S.H.; Huang, T.S.; Yen, J.Y. Tracking control of shape-memory-alloy actuators based on self-sensing feedback and inverse hysteresis compensation. *Sensors* **2009**, *10*, 112–127. [CrossRef] [PubMed]
45. Senthilkumar, P.; Dayananda, G.; Umapathy, M.; Shankar, V. Experimental evaluation of a shape memory alloy wire actuator with a modulated adaptive controller for position control. *Smart Mater. Struct.* **2011**, *21*, 015015. [CrossRef]
46. Dunbar, B. NASA Tests New Alloy to Fold Wings in Fligh. 2020. Available online: https://www.nasa.gov/centers/armstrong/feature/nasa-tests-new-alloy-to-fold-wings-in-flight.html (accessed on 20 March 2023).
47. Jeong, J.; Hyeon, K.; Han, J.; Park, C.H.; Ahn, S.Y.; Bok, S.K.; Kyung, K.U. Wrist assisting soft wearable robot with stretchable coolant vessel integrated SMA muscle. *IEEE/ASME Trans. Mechatronics* **2021**, *27*, 1046–1058. [CrossRef]